Available online at www.sciencedirect.com

ScienceDirect

Advances in Space Research 73 (2024) 945–957

ADVANCES IN SPACE RESEARCH (a COSPAR publication)

www.elsevier.com/locate/asr

Np-Fe^0 addition affects the microstructure and composition of the microwave-sintered lunar soil simulant CLRS-2

Tian Zhang [a,b], Hong Tang [a,c,d,*], Xiongyao Li [a,c,d], Chuanjiao Zhou [a,b], Wen Yu [a,c,d], Bing Mo [a,c,d], Jianzhong Liu [a,c,d], Xiaojia Zeng [a,d]

[a] Center for Lunar and Planetary Sciences, Institute of Geochemistry, Chinese Academy of Sciences, Guiyang 550081, China
[b] College of Earth and Planetary Sciences, University of Chinese Academy of Sciences, Beijing 100049, China
[c] CAS Center for Excellence in Comparative Planetology, Hefei 230026, China
[d] Key Laboratory of Space Manufacturing Technology, Chinese Academy of Sciences, Beijing 100094, China

Received 7 December 2022; received in revised form 12 August 2023; accepted 17 August 2023
Available online 23 August 2023

Abstract

Microwave sintering is a key technology for future lunar habitats, which has been verified by various lunar soil simulant experiments. However, nanophase iron (np-Fe^0), a unique component of the real lunar regolith, has been ignored in previous studies of the microwave sintering of lunar soil simulants. In this study, microwave-sintering experiments of lunar soil simulant CLRS-2 with and without np-Fe^0 at different temperatures were conducted. A comparison of the microstructure and chemical composition of sintered products indicates that all products of samples with 1.0 wt% np-Fe^0 exhibit better properties than those without np-Fe^0 after heating at equivalent temperatures. Adding np-Fe^0 to the lunar soil simulant CLRS-2 couples well with microwaves, which may increase the real heating temperature in a sample, resulting in the product being solidified at 700 °C and a relatively dense product forming at 900 °C, thus improving the sintering efficiency. This study suggests that microwave sintering is an effective potential technology for future lunar habitats and road hardening because of the wide distribution of np-Fe^0 in the lunar regolith. The technical parameters given in this study can provide an important guide for future lunar construction by microwave sintering.

Keywords: Nanophase iron (np-Fe^0); Lunar habitats; Lunar soil simulant; Microwave sintering

1. Introduction

Building a permanent lunar habitat is critical for humans to exploit lunar resources and explore deep space. Because transporting materials from Earth is costly, it is sensible to consider in-situ resource utilization technologies that use the local lunar regolith to develop lunar habitats (Duke et al., 2003). Therefore, a series of technologies, including microwave sintering (Hill et al., 2005, Kim et al., 2021; Lim et al., 2021; Srivastava et al., 2016; Taylor and Meek, 2005; Taylor et al., 2003, 2006; Zhou et al., 2021), solar sintering (Nakamura and Senior, 2005, 2008), laser sintering (Fateri and Gebhardt, 2015), and plasma sintering (Zhang et al., 2020, 2021), have been proposed over past decades (Farries et al., 2021). Microwave sintering is distinguished among these technologies by its rapid sintering, volumetric heating, and energy efficiency (Oghbaei and Mirzaee, 2010; Taylor and Meek, 2003, 2005; Taylor et al., 2006). The potential application of microwave sintering has been verified by previous simulation experiments and numerical modeling with lunar soil simulants, and the effects of different compositions, temperatures, and input powers on the sintered products have

* Corresponding author.
E-mail address: tanghong@vip.gyig.ac.cn (H. Tang).

https://doi.org/10.1016/j.asr.2023.08.029
0273-1177/

been discussed (Allan et al., 2013; Lim and Anand, 2019; Zhou et al., 2021).

It should be noted that previous studies of microwave sintering by various lunar soil simulants have ignored a unique property in the actual lunar regolith—nanophase iron (np-Fe^0) (Basu, 2005; James et al., 2003; Taylor and Liu, 2010; Taylor and Meek, 2005). This np-Fe^0 is thought to form by vapor deposition from micrometeorite bombardment and sputtering deposition by solar wind implantation (Basu, 2005, Gu et al., 2022; Hapke, 2001; Hapke et al., 1975; Loeffler et al., 2009; Sasaki et al., 2001; Weber et al., 2020; Yamada et al., 1999). It is widely distributed and exhibits different size characteristics in the rims of lunar soil particles and agglutinate glasses (Basu, 2005; Guo et al., 2022; James et al., 2003; Pieters and Noble, 2016; Tang et al., 2011). The np-Fe^0 in the rims of lunar soil particles has a diameter of 3–33 nm, while in agglutinate glasses, its diameter can be > 100 nm, sometimes up to nearly 1 μm (Basu, 2005; Gu et al., 2022; James et al., 2003; Pieters and Noble; 2016, Tang et al., 2011). In addition, the contents of np-Fe^0 in lunar mare and highland areas are different; in the highland, the np-Fe^0 content is approximately 0.7 wt%, whereas, in the mare, it is close to 1.0 wt% (Mo et al., 2022; Morris, 1980; Tang et al., 2011). Taylor and Meek (2005) performed microwave-sintering experiments on Apollo samples and speculated that np-Fe^0 could couple well with microwaves, which could markedly influence the microwave-sintering process and the performance of sintered products (Taylor and Liu, 2010; Taylor and Meek, 2005; Taylor et al., 2006).

The microwave sintering of real lunar samples provides only preliminary data and does not provide a detailed investigation of the relationship between np-Fe^0 and sintered products. Simultaneously, the influence of np-Fe^0 cannot be reflected by microwave-sintering lunar soil simulants. Here, to understand the effect of np-Fe^0 on the characteristics of microwave-sintering products, commercial np-Fe^0 was added to the lunar soil simulant CLRS-2 to conduct microwave-sintering experiments, and the microstructure, composition, and valence of Fe in the resulting products were analyzed.

2. Samples and experiments

2.1. Sample preparation

The lunar mare soil simulant CLRS-2 developed by the Institute of Geochemistry, Chinese Academy of Sciences, was used for the microwave-sintering experiments. The main minerals in CLRS-2 are plagioclase feldspar, olivine, pyroxene, and ilmenite, and the chemical composition is shown in Table 1. The np-Fe^0 was provided by Jiangsu Leiming New Materials Technology Co. Ltd., and its X-ray diffraction (XRD) patten and scanning electron microscope (SEM) image are shown in Fig. 1. To reduce absorbed water and lower weighting error, all the lunar soil simulants and corundum crucibles used in this study were baked at 120 °C for approximately 24 h. Because np-Fe^0 is very active, all samples were prepared in a glove box and transferred in a sealed box filled with high-purity Ar before being microwave sintered. Each corundum crucible (50 × 20 × 20 mm) held 10 g of sample material; approximately 1.0 wt% of np-Fe^0 was also required. Therefore, approximately 9.9 g of CLRS-2 and 0.1 g of np-Fe^0 were weighed, using an electronic scale with a one-in-ten-thousand accuracy. To avoid spontaneous combustion or mass loss of np-Fe^0 in the mixing process, a multi-layer structure was used to prepare the samples. One quarter of the CLRS-2 sample was placed flat in a corundum crucible, followed by one third of the weighed np-Fe^0, which was evenly spread over the CLRS-2 sample surface. This process was repeated until the crucible contained four layers of CLRS-2 and three layers of np-Fe^0. A total of six samples were prepared using this method. Although the multi-layer structure is different from the real situation, the cross section of sintered products does not show differences in structure and composition (**Figure S1**), indicating that this method can be used to discuss the microwave-sintering process of real lunar soil. As a control group, six 10-g pure CLRS-2 samples without np-Fe^0 were also prepared in corundum crucibles. The samples with np-Fe^0 were labelled #0702, #0802, #0902, #1002, #1102, and #1202, while the samples without np-Fe^0 were labelled #0701, #0801, #0901, #1001, #1101, and #1201. The first two numbers of each sample label represent the different sintering temperatures; that is, 07, 08, 09, 10, 11, and 12 correspond to 700, 800, 900, 1000, 1100, and 1200 °C, respectively. The selected sintering temperatures in this experiment are based on previous research and the composition of the lunar soil simulant CLRS-2 (Lei et al., 2020).

2.2. Microwave-sintering process

To minimize oxidation, the prepared samples were transported from the glove box to the microwave-sintering apparatus in a box filled with high-purity Ar. Fig. 2 shows the basic arrangement of the microwave furnace, which provides microwave energy through two magnetrons. Samples in crucibles (50 × 20 × 20 mm), one with and one without np-Fe^0, were protected by larger crucibles (60 × 30 × 30 mm). The two samples were simultaneously placed into a mullite container (102 × 102 × 30 mm) and then heated on the same magnetron side. The temperature during the heating process was measured by a Pt–Rh thermocouple above the samples. The insulation material around the sample cavity was composed of alumina fibers. To reduce the oxidation of samples during the heating process, the furnace wall was closed tightly, and the pump was opened to exclude air in the furnace until the pressure was approximately 3000 Pa. After this point, a mixed flow of 96% N and 4% Ar was pumped into the furnace until the pressure within the furnace was just higher than atmospheric pressure, and then this mixture was pumped away

Table 1
Chemical composition of lunar soil simulant CLRS-2 measured by X-ray fluorescence.

Chemical composition	SiO_2	Al_2O_3	Fe_2O_3	MgO	CaO	Na_2O	K_2O	MnO	P_2O_5	TiO_2
Contents(wt%)	40.73	12.33	18.04	7.55	10.25	2.42	0.77	0.20	0.16	6.58

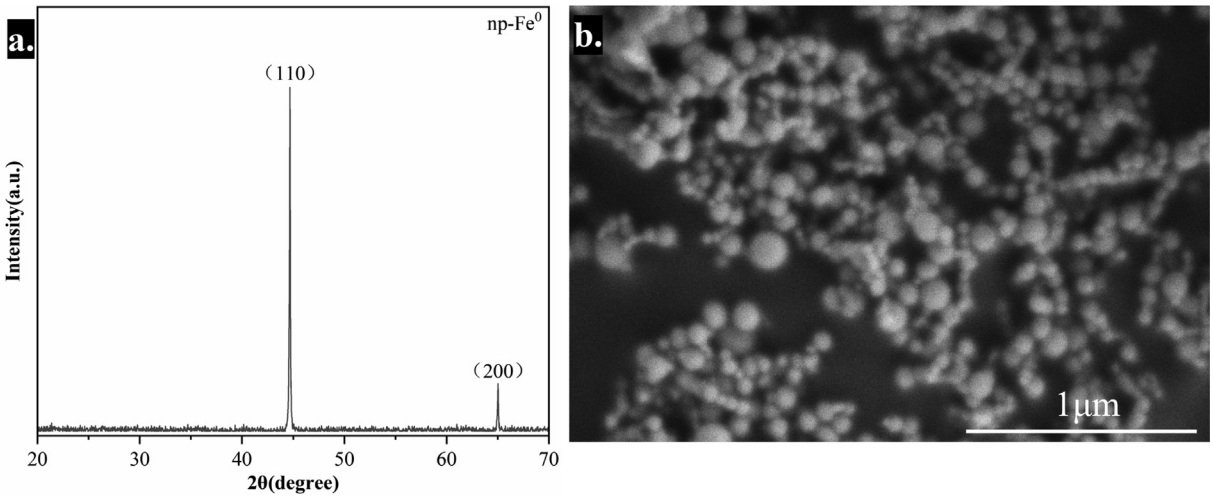

Fig. 1. X-ray diffraction (XRD) pattern and scanning electron microscope (SEM) image of np-Fe^0. **(a)** XRD pattern showing that the np-Fe^0 has a high degree of purity. **(b)** SEM image of np-Fe^0 showing that it has a diameter range of dozens to hundreds of nanometers.

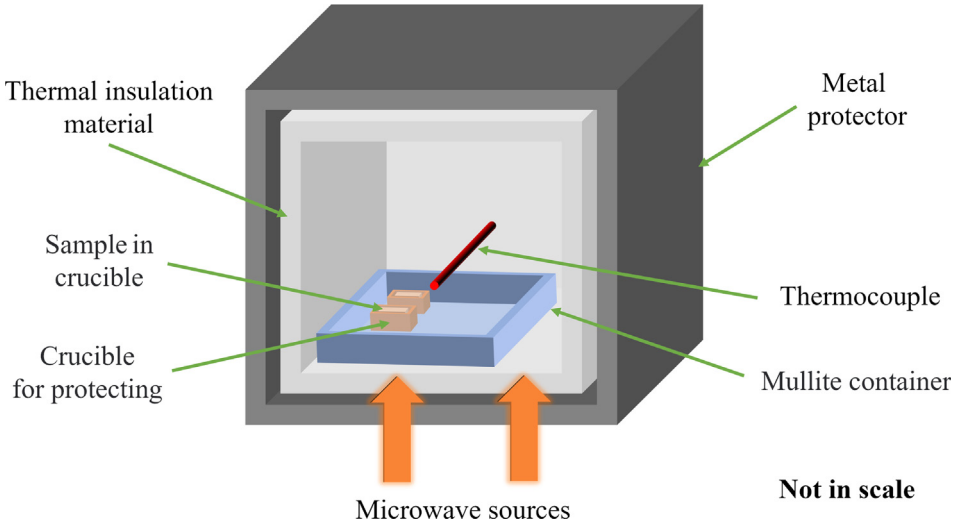

Fig. 2. Schematic diagram of microwave sintering.

again. This process was repeated three times to maintain the pressure in the furnace at a level a little higher than atmospheric pressure during the microwave heating process. Subsequently, the parameters for automatic sintering were set; the key parameters are summarized in Table 2. The heating process can be described as follows: First, from room temperature to 300 °C, the heating rate was set at 7.5 °C/min with an input power of 1300 W; this was used for preheating the furnace. Next, the power was increased to 1500 W to arrive at the target temperature at a rate of 6.25 °C/min. Six groups of samples (each included one sample with and one without np-Fe^0) were heated to different temperatures, ranging from 700 to 1200 °C, at intervals of 100 °C. The sintering process requires approximately 60 min of holding time at the target temperature, using an input power of 1500 W. After sintering, the input power was adjusted to 1000 W and the samples were cooled to 600 °C at a rate of 5 °C/min. The heated products were then cooled naturally to a safe temperature for removal from the furnace. Finally, the products were separated from the crucibles using a diamond liner cutter. The characteristics of the products are shown

Table 2
Sintering parameters.

Samples	Target Temperature (°C)	Power to 300 °C (W)	Power to Target Temperature and holding (W)	Power to Cooling Temperature (W)	Heating Rate (°C/min)	Holding Time (min)	Time of Cooling to 600 °C (min)
#0701 & #0702	700	1300	1500	1000	7.5 to 6.25	60	20
#0801 & #0802	800	1300	1500	1000	7.5 to 6.25	60	40
#0901 & #0902	900	1300	1500	1000	7.5 to 6.25	60	60
#1001 & #1002	1000	1300	1500	1000	7.5 to 6.25	60	80
#1101 & #1102	1100	1300	1500	1000	7.5 to 6.25	60	100
#1201 & #1202	1200	1300	1500	1000	7.5 to 6.25	60	120

in Fig. 3, and their basic information is summarized in Table 3. The phases, chemical composition, and microstructure of the sintered products were analyzed.

2.3. Analysis methods

Before sintering, the CLRS-2 and np-Fe^0 were analyzed by XRD with Ni-filtered Cu radiation at 40 kV and 40 mA, and the morphology of the np-Fe^0 was also observed using an SEM. Several analytical methods were used to compare the properties of the microwave-sintered products. The microstructure and composition of the sintered products were analyzed using an SEM with an energy-dispersive X-ray spectrometer. The back-scattered electron images of the sintered products were taken with a beam current of 0.2nA and an accelerating voltage of 15 kV. The mineral phases of the sintered products were determined using XRD with Ni-filtered Cu radiation at 40 kV and 40 mA. These analyses were conducted at the Institute of Geochemistry, Chinese Academy of Sciences. The relative contents of the different valence states of Fe in the sintered products were analyzed at room temperature using a Mossbauer spectrometer with ^{57}Co (Rh) as a radioactive source at the Dalian Institute of Chemistry and Physics, Chinese Academy of Science. To observe the internal microstructure of the sintered products, a high-resolution X-ray tomographic microscope with a voltage of 50 kV and power of 4 W was used to systematically perform a detailed three-dimensional scan of the sintered products at the Nanjing Institute of Geology and Paleontology, Chinese Academy of Sciences.

3. Results

3.1. Morphology and structure of sintered products

The appearance characteristics of the products are shown in Fig. 3. After heating at 700 and 800 °C, products #0701 and #0801 remained in powder form. When heated at 900 °C, product #0901 solidified with a rough surface containing many pores. However, when heated at only 700 °C, product #0702 solidified and contained relatively few visible pores. After sintering at 900 °C, product #0902 presented a harder surface compared with product #0901. Generally, after heating at a given temperature, all products of samples with np-Fe^0 had harder surfaces and fewer pores compared with those lacking np-Fe^0.

Fig. 4 shows the microscopic structures of the products of samples with and without np-Fe^0 after heating at different temperatures. At 900 °C, product #0901 presented an accumulated solid phase, and most minerals were agglutinated in their original form; this product contained many spherical pores, the largest of which exceeded 300 μm. Several large minerals with high melting points, such as ilmenite and olivine, remained unaffected by sintering at 1000 °C in product #1001, while other minerals with low melting points melted and some minerals recrystallized.

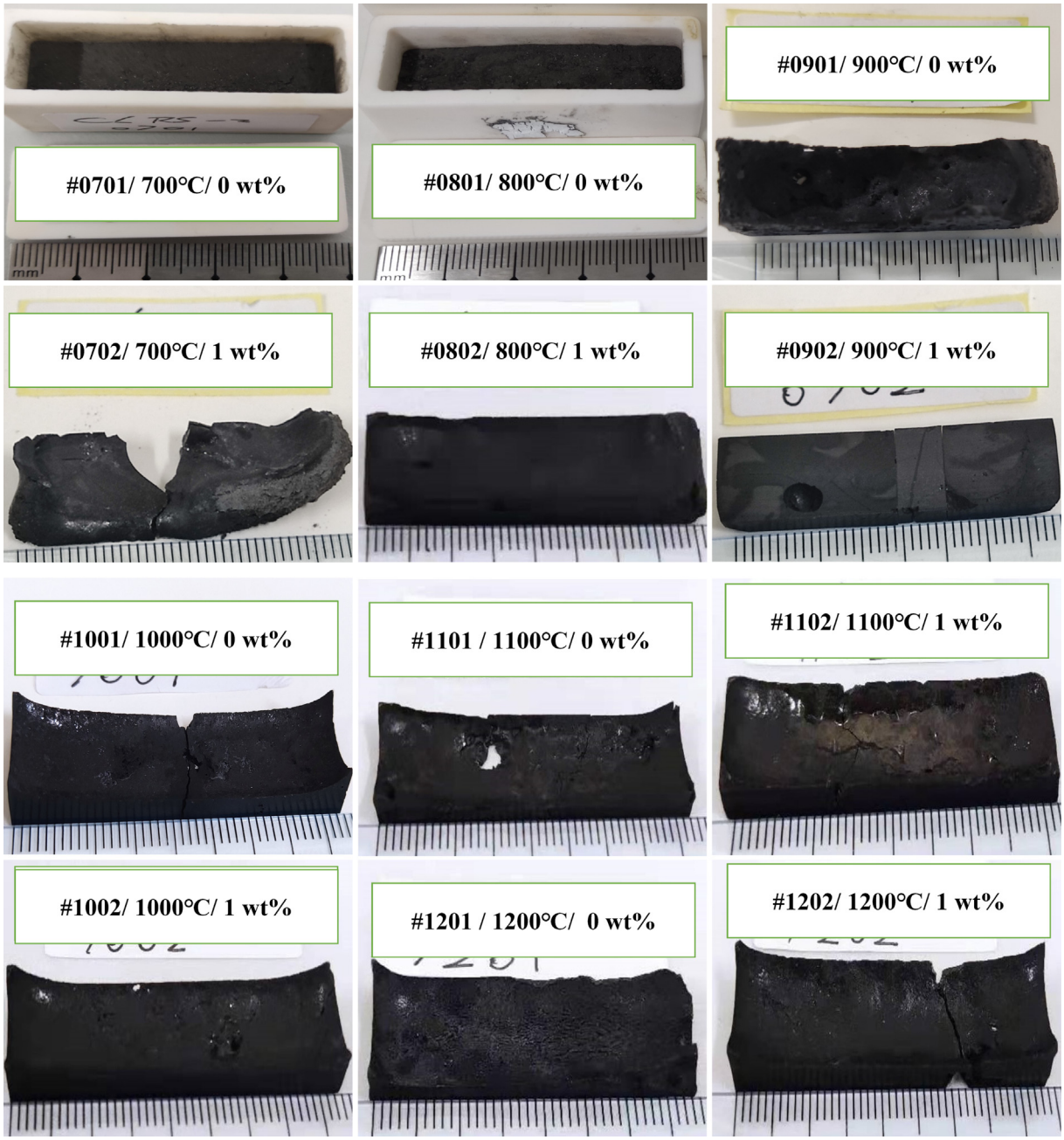

Fig. 3. Characteristics of sintered products. Products of samples with np-Fe^0 were labeled using numbers ending "02", and the content of np-Fe^0 was 1.0 wt%. Products of samples without np-Fe^0 were labeled using numbers ending "01", and the content of np-Fe^0 was 0 wt%.

When the temperature was increased to 1100 °C, product #1101 transformed into glass with numerous irregular micro-scale pores. After sintering at 1200 °C, product #1201 contained some micro-scale pores and many needle-like plagioclase and pyroxene grains formed by recrystallization. Generally, with increasing sintering temperature, the products of samples without np-Fe^0 showed fewer and smaller pores, the minerals gradually melted, and the amount of recrystallized plagioclase gradually increased.

However, at just 700 °C, product #0702 solidified; it contained randomly distributed spherical pores, the largest being almost 50 μm in diameter. Most of the minerals in #0702 were agglutinated; although there was no obvious recrystallization, some melted rims could be observed at the edges of the minerals. The microstructure of this product was similar to that of product #0901, which was sintered at 900 °C, but the pores of #0702 were much smaller. Similar to product #1001 sintered at 1000 °C, product #0802 sintered at 800 °C underwent melting, decomposition, and partial recrystallization, except for some olivine and ilmenite grains, and other minerals. In addition, large olivine and ilmenite grains had distinct melted rims. After sintering at 900 °C, product #0902 showed evident

Table 3
Summary of products after heating in a microwave furnace.

Samples	Temperature (℃)	State	Bond to the Crucible	Size (l*w*h cm)	Density (g/cm^3)
#0001	Room temperature	_	_	_	_
#0701	700	Loose	No	_	_
#0702	700	Partial sintered	Little	4.1*0.7*0.4	3.11
#0801	800	Loose	No	_	_
#0802	800	Sintered	Little	4.2*1.3*0.5	3.20
#0901	900	Partial sintered	Little	3.9*0.7*0.5	2.85
#0902	900	Sintered	A lot	4.0*1.0*0.5	3.22
#1001	1000	Sintered	A Lot	4.3*1.2*0.4	3.09
#1002	1000	Sintered	A lot	4.2*1.3*0.5	3.20
#1101	1100	Sintered	A lot	4.2*1.3*0.3	3.15
#1102	1100	Sintered	A lot	4.3*1.3*0.4	3.30
#1201	1200	Sintered	A lot	3.8*1.2*0.3	3.23
#1202	1200	Sintered	A lot	4.4*1.2*0.5	3.23

vitrification with a few recrystallized minerals; only a crack and several small pores were observed. With temperatures increasing to 1000 °C and 1100 °C, recrystallization of the minerals in the sintered products of samples with np-Fe^0 became more evident; in particular, plagioclase grains appeared as needles. Meanwhile, the pores in products #1002 and #1102 also increased. However, the needle-like minerals and pores were reduced in the product until the sintering temperature reached 1200 °C.

Comparing the differences between the sintered products of samples with and without np-Fe^0 reveals that, at equivalent heating temperatures, products of samples with np-Fe^0 had fewer and smaller pores. Computed tomography (CT) images of the potential pores and cracks in products sintered at 900 °C are shown in Fig. 5. Product #0901 contained many pores, whereas, at the same temperature, product #0902 contained a crack but fewer internal pores. In general, when the heating temperature of the sample without np-Fe^0 was higher than that of the sample with np-Fe^0, a similar microstructure was observed in their sintered products. Product #0901 sintered at 900 °C and product #0702 sintered at 700 °C had similar mineral arrangements and spherical pores; however, the latter had fewer and smaller pores than did the former. In addition, even though similar vitrification could be observed in product #1101 sintered at 1100 °C and product #0902 sintered at 900 °C, the latter showed a higher degree of vitrification and fewer pores compared with the former.

3.2. Phases of sintered products

Fig. 6 shows the XRD patterns of lunar soil simulant CLRS-2 and the sintered products. Disregarding glass, metallic Fe, and other low-content minerals such as magnetite, which went undetected, the crystalline phases of all products primarily comprised plagioclase, pyroxene, ilmenite, and olivine; these correspond to the minerals shown in Fig. 4. Fig. 6**a** shows the peak intensities of the main components in the products of samples without np-Fe^0, after sintering at different temperatures. The intensity of plagioclase near 28° weakened considerably at 1000 °C but recovered at 1200 °C. This phenomenon is consistent with that shown in Fig. 4, in which the plagioclase began to melt at 1000 °C, mostly became glass at 1100 °C, then recrystallized to numerous needle-like plagioclase crystals at 1200 °C. Other minerals also showed similar trends. For pyroxene, the intensity of the main peak at 30° weakened markedly and the secondary peak near 35° disappeared with increasing temperature. For ilmenite, the peak intensity in product #1101 that was sintered at 1100 °C was evidently the weakest.

Fig. 6**b** shows the peak intensities of the main components in the products of samples with np-Fe^0 added, after sintering at different temperatures. Above 700 °C, the peak intensities of plagioclase, pyroxene, and ilmenite started to decrease and reached their lowest values at 900 °C. The intensities recovered at 1000 °C and then did not change significantly as the temperature further increased. Notably, at 900 °C, many weak mineral peaks disappeared, including the olivine peaks. This result is consistent with the phenomenon of vitrification in product #0902 that was sintered at 900 °C, as shown in Fig. 4.

3.3. Iron content in different phases of sintered products

Fig. 7 shows the relative Fe contents with different valence states in the various phases of CLRS-2 and the sintered products, as characterized by Mössbauer spectroscopy. Based on previous studies (Dyar et al., 2006; Herzenberg, 1970; Herzenberg and Riley, 1970,1971; Rancourt et al., 1994; Stevens et al., 1998) and the compositions of the products described above, the main Fe-bearing phases were identified as ilmenite, Fe-silicate, and magnetite; no metallic iron was observed.

Fig. 7**a** shows the relative Fe content in the different phases of CLRS-2 and the products of samples without np-Fe^0. From 700 to 800 °C, the relative Fe content in the different phases of the heated products (#0701 and #0801) was nearly the same as that of CLRS-2, which is consistent with the fact that the two products showed no consolidation. When the temperature increased to 900 °C, the relative Fe content in product #0901 changed mark-

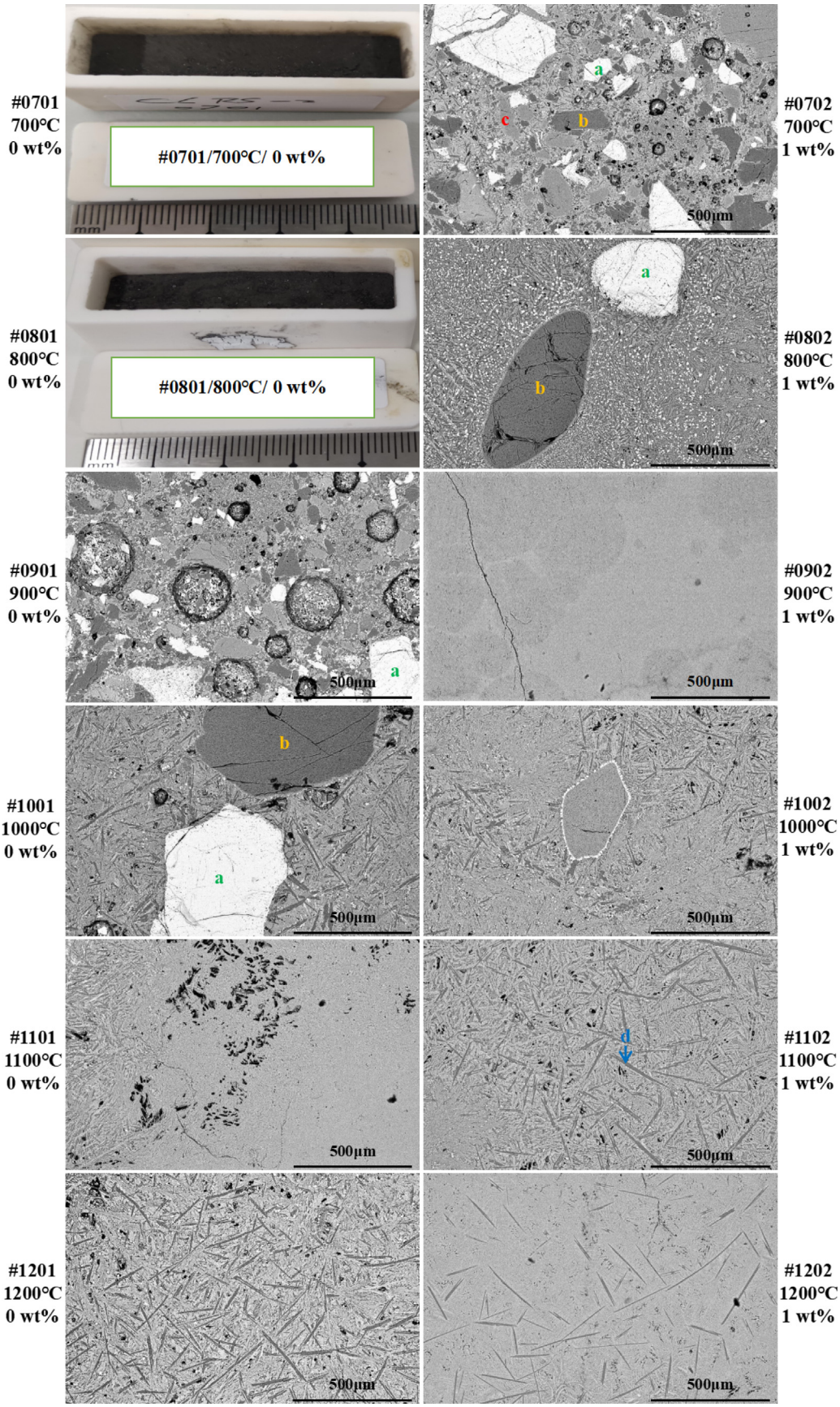

Fig. 4. Back-scattered electron images of sintered products. The main phases include: **a** = ilmenite (**Ilm**), **b** = olivine (**Ol**), **c** = Pyroxene (**Px**), and **d** = needle-like plagioclase (**Pl**).

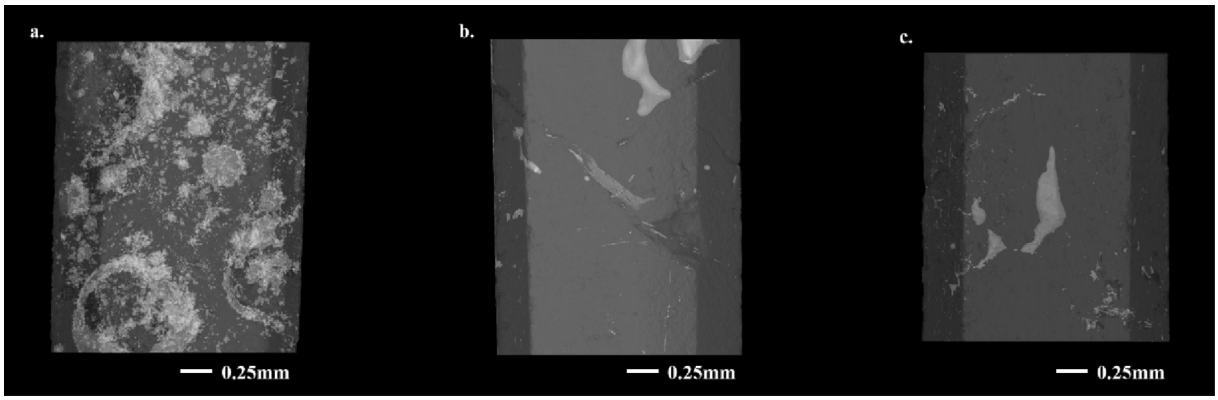

Fig. 5. Computed tomography images of sintered products. **(a)** Product #0901 sintered at 900 °C. **(b)** Product #0902 sintered at 900 °C. **(c)** Product #1101 sintered at 1100 °C. These CT images were acquired by adjusting the transparency of sintered products; hence, the white areas indicate the distribution of pores and fractures.

edly. Magnetite Fe^{2+} and Fe^{3+} signals could not be detected; however, the silicate Fe^{2+} and Fe^{3+} contents increased substantially, to approximately twice those of the products #0701 and #0801. Conversely, the ilmenite Fe^{2+} content decreased at this time. When the temperature increased to 1000 °C, the silicate and ilmenite Fe^{2+} contents increased slightly, while the silicate Fe^{3+} content decreased markedly. From 1100 to 1200 °C, the relative Fe content of different valence states in the two heated products #1101 and #1201 basically remained stable.

Fig. 7**b** shows the relative Fe content in the different phases of CLRS-2 and the products of samples with np-Fe^0. When heated to just 700 °C, no magnetite Fe^{2+} or Fe^{3+} signals were detected in product #0702 and the silicate Fe^{2+} content increased substantially, to nearly twice that of CLRS-2. As temperature increased, the Fe content in the different phases was more stable than that of the products without np-Fe^0.

Fig. 7**c** shows the Fe^{2+}/Fe^{3+} ratio in the silicate phases of the heated products. For products of samples without np-Fe^0, the Fe^{2+}/Fe^{3+} ratio after heating at 700–900 °C changed little compared with that of CLRS-2. The ratio increased substantially at 1000 °C, to nearly three times that of the product sintered at 900 °C. This ratio then dropped by a third and remained stable at 1100 °C and 1200 °C. However, after heating at different temperatures, the Fe^{2+}/Fe^{3+} ratios in products of samples with np-Fe^0 were different from those of samples without np-Fe^0. After heating to just 700 °C, the Fe^{2+}/Fe^{3+} ratio in product #0702 was nearly four times that of CLRS-2; it changed little from 800 to 900 °C, then decreased substantially at 1000 °C, to nearly half the value observed at 900 °C. The ratio then increased and peaked at 1100 °C before dropping slightly at 1200 °C. In general, except for the products sintered at 1000 °C, it was evident that all products of samples without np-Fe^0 had lower ratios than products of samples with np-Fe^0 after sintering, with differences of 2–3 times.

4. Discussion

4.1. Influence of np-Fe^0 on the structure and composition of microwave-sintered products

Comparing the structure and composition of the heated products of samples with and without np-Fe^0, sintered at equivalent temperatures, evident differences were observed. A notable phenomenon is the appearance of pores, as shown in Fig. 4, which are caused by the vaporization of different types of water and other low-melting-point materials (Lei et al., 2020). Products of samples with and without np-Fe^0 exhibited distinct characteristics at equivalent heating temperatures, and this single variable indicates that these differences arise from the added np-Fe^0 coupling well with microwave energy.

Previous studies have classified materials in the microwave field into three categories: 1) reflector, e.g., bulk metal, which makes microwaves reflect and is therefore impenetrable; 2) transparent, e.g., glass, which microwaves pass through without loss; and 3) absorber, e.g., water and some minerals, where microwaves are absorbed (Oghbaei and Mirzaee, 2010; Taylor and Meek, 2003; Taylor et al., 2006). Even though bulk metal is a strong reflector of microwaves, many studies have found that metal powder can be an excellent microwave absorber when its size is smaller than the skin depth of bulk metal (Mondal et al., 2008, 2010; Taylor et al., 2006); the skin depth can be calculated as follows (Gupta and Wong, 2007; Sun et al., 2016):

$$d = \frac{\sqrt{2\rho}}{\omega\mu_0\mu'}$$

where d, ρ, ω, μ_0, and μ' represent the skin depth, resistivity of the material, angle frequency, magnetic permeability, and relative magnetic constant, respectively. The skin depth of bulk Fe metal is approximately 1.3 μm (El

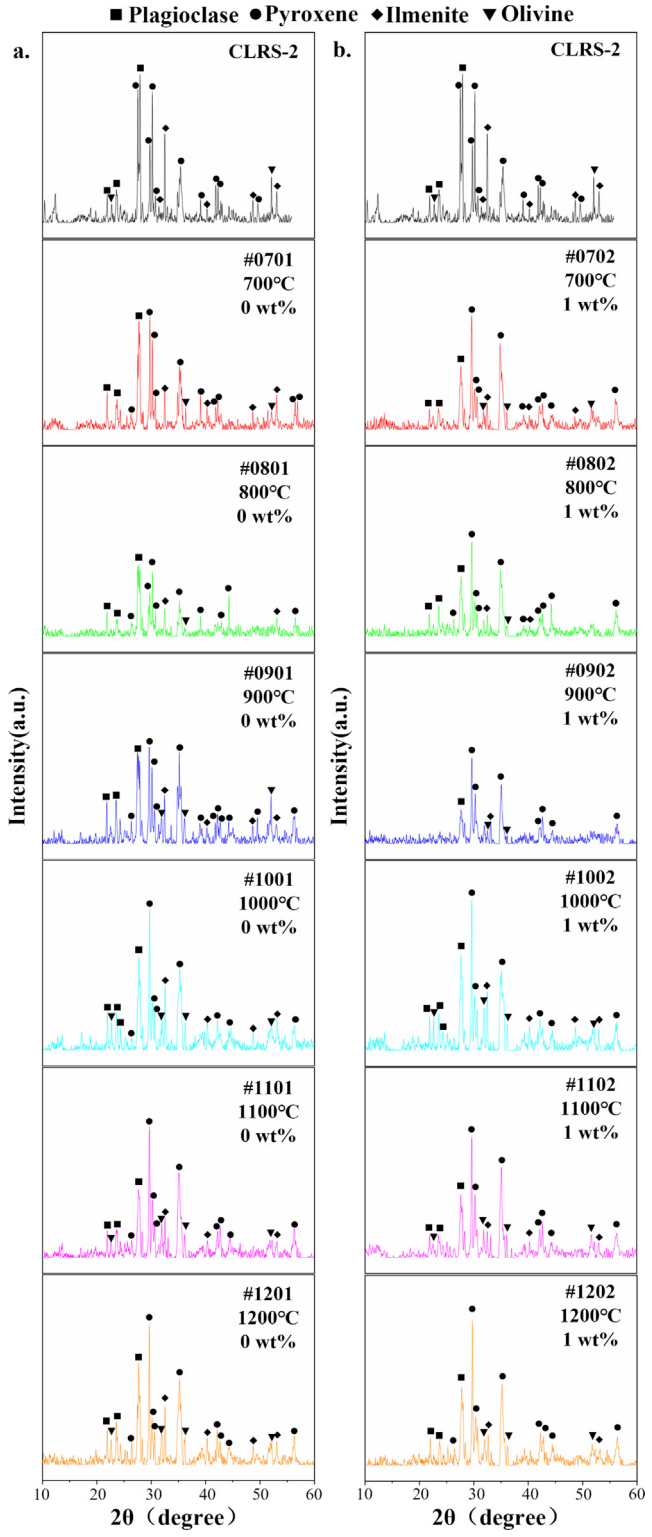

Fig. 6. X-ray diffraction patterns of sintered products. **(a)** Comparison of the XRD patterns of CLRS-2 and products of samples without np-Fe^0 after sintering at different temperatures. **(b)** Comparison of the XRD patterns of CLRS-2 and products of samples with np-Fe^0 after sintering at different temperatures.

Khaled et al., 2018; Sun et al., 2016), which is larger than the diameter of the np-Fe^0 used in the experiments, as well as that of np-Fe^0 in actual lunar soil (Basu, 2005; Gu et al., 2022; James et al., 2003; Pieters and Noble, 2016; Tang et al., 2011).

To better understand the interaction of microwaves with metal, three mechanisms (magnetic loss, conductive loss, and dielectric loss) have been proposed in past decades (Cheng et al., 2002; Gupta and Wong, 2007; Luo et al., 2004; Rybakov et al., 2006; Rybakov and Volkovskaya, 2019; Zhang et al., 2018). Previous studies have attributed the heating absorption mechanism of materials that interact with microwaves to dielectric loss (Oghbaei and Mirzaee, 2010); however, such a theory is not well suited for metal heating in microwave fields (Gupta and Wong, 2007). Research into metallic Fe and Fe-oxide powders in separate magnetic (H) and electric (E) microwave fields (**Figure S2**) indicates that metallic Fe is better heated in a H microwave field (Cheng et al., 2002; Gupta and Wong, 2007). Therefore, the main mechanisms by which np-Fe^0 converts microwave energy into thermal energy should be magnetic and conductive loss (Anzulevich et al., 2017; Gupta and Wong, 2007; Rybakov et al., 2006; Rybakov and Volkovskaya, 2019; Sun et al., 2016; Zhang et al., 2018; Zhou et al., 2017). However, herein, no metallic Fe was detected in sintered products by Mössbauer spectroscopy, which means that the added np-Fe^0 was likely oxidized during the heating process. Moreover, the sintered products were black, different from the red color of previous products sintered in air, indicating that oxidation in our experiments is not obvious, and the oxides may mainly be FeO (**Figure S3**). Based on the heating behavior of metallic Fe and Fe-oxides in H and E fields (**Figure S2**), np-Fe^0 can quickly reach a high temperature via magnetic loss during microwave heating, while FeO after the oxidation of np-Fe^0 during the heating process can promote heating in the form of dielectric loss. Consequently, the added np-Fe^0, although it may be oxidized to FeO, plays the role of an extra heating absorber in samples during the microwave-sintering process. At equivalent microwave-heating conditions, the actual temperature of samples with np-Fe^0 might be higher than that of samples without np-Fe^0, causing differences in their products.

Adding np-Fe^0 to the lunar soil simulant has a good absorption effect and converts the microwave energy into a large amount of heat after absorbing microwaves, causing the product of the sample with np-Fe^0 to enter the solid phase after heating at 700 °C. The heat generated by the sample with np-Fe^0 in the microwave field at 800 °C was sufficient to melt most of the minerals, except for some minerals with high melting points; it can be described as partially melted, further improving the compactness of the product. At 900 °C, adding np-Fe^0 to the lunar soil simulant accelerated the melting of minerals; simultaneously, the short cooling period promoted vitrification; accordingly, the structure of this product was more compact. With increasing temperature, almost all minerals completely melted; however, some minerals recrystallized because the cooling time increased. Adding np-Fe^0 to the lunar soil simulant plays a key role in heat conduction dur-

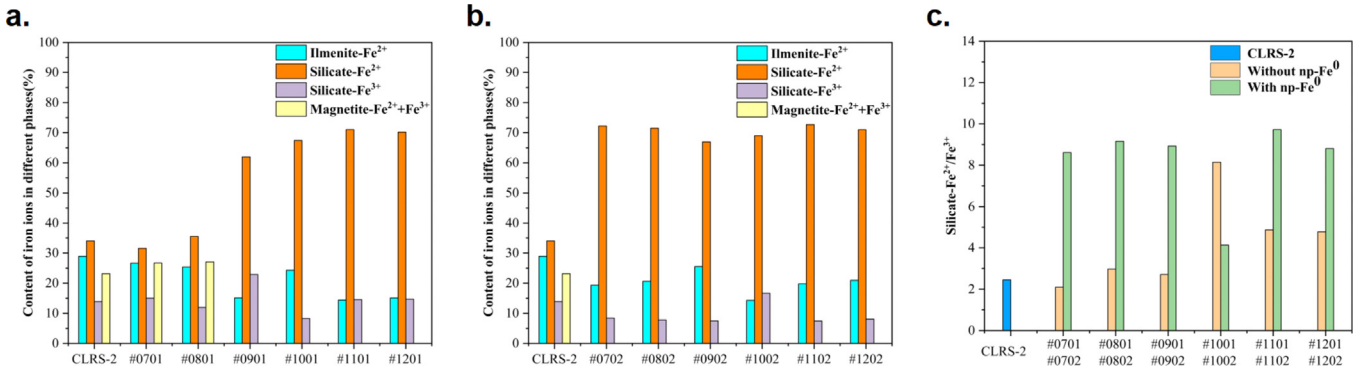

Fig. 7. Relative content of Fe in different phases of CLRS-2 and sintered products. (a) Comparison of the Fe content of CLRS-2 and the products of samples without np-Fe^0. (b) Comparison of the Fe content of CLRS-2 and the products of samples with np-Fe^0. (c) Ratio of Fe^{2+}/Fe^{3+} in silicate phases of CLRS-2 and sintered products.

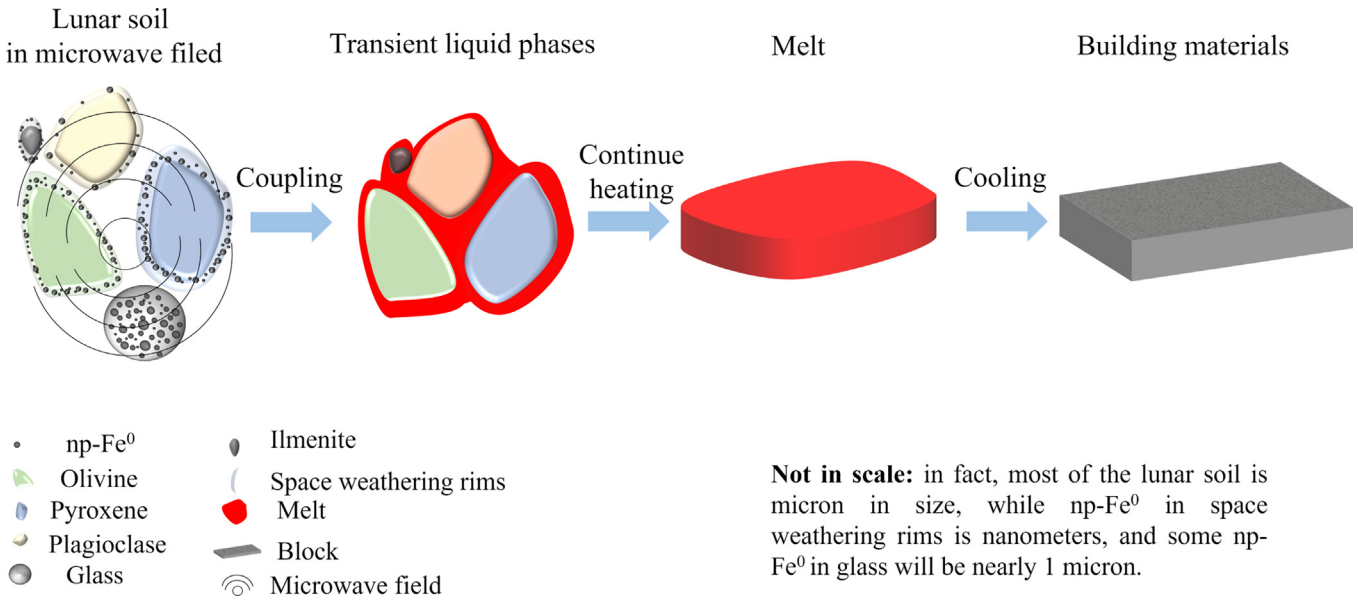

Fig. 8. Schematic diagram of microwave-sintering of lunar soil. Space weathering rims and agglutinate glass are transparent to microwaves and have no specific melting point, thus are easily melted by the heat produced by np-Fe^0 coupling with microwaves. Therefore, transient liquid phases can be formed, and the lunar soil can be sintered.

ing microwave sintering, resulting in the sintered products of samples with np-Fe^0 having greater compaction as well as smaller and fewer bubbles compared with the products of samples without np-Fe^0, when heated at equivalent temperatures. Adding np-Fe^0 to the lunar soil simulant converts microwave energy into heat, promoting the melting of silicate minerals and ilmenite. In real lunar soil, the np-Fe^0 heated by microwaves also plays the role of a transient liquid phase (Taylor and Meek, 2005), which can induce lunar soil particles to agglutinate and consolidate.

Previous studies have also found that metal powder accelerates series reaction in a microwave field (Whittaker and Mingos, 1993, 1995), and such powders have been widely used to synthesize various materials (Vinothini et al., 2010; Yun et al., 2019). In this study, np-Fe^0 added to the lunar soil simulant caused distinct degrees of melting and recrystallization of the products at different temperatures, thus changing the composition of the products. Although most of the minerals in product #0702 did not melt after heating at 700 °C, many rims appeared around the edges of these minerals, indicating that partial reaction and melting had occurred. Plagioclase, pyroxene, and small olivine and ilmenite crystals in the sample with np-Fe^0 melted after heating at 800 °C, leaving some large olivine and ilmenite crystals with melted rims. At 900 °C, product #0902 showed evident vitrification, suggesting that almost all the minerals had melted, and a small amount of the minerals had recrystallized during cooling. However, the heating temperature was lower than the actual melting points of most of these minerals, suggesting that np-Fe^0 added to the lunar soil simulant might raise the temperature locally to reach the melting points of these minerals. However, this

hypothesis requires further investigation using more precise temperature measurement methods. Fine particles of Fe–Ti-oxide were dispersed within the products after heating, indicating that part of the reaction took place at a high temperature to enable its recrystallization. The length of needle-like plagioclase extended with higher temperatures and increased cooling time. However, other minerals with high melting points are difficult to recrystallize at the same cooling time. This is the main reason why needle-like plagioclase is the most obvious recrystallization phases in sintered products.

Adding np-Fe^0 to the lunar soil simulant couple well with microwaves, causing differential phase melting, element migration, and valence changes. Many rims appeared at the edges of minerals in the products of samples with np-Fe^0 after sintering at 800 °C; this may be the result of the continuous migration of elements during sintering reactions. In addition, the valence state and relative content of Fe changed markedly in these products. The higher temperature conditions created by the addition of np-Fe^0 to the lunar soil simulant may promote the migration of elements from decomposing magnetite to the silicate phase by isomorphism or other mechanisms. This could be the main reason why the relative Fe^{2+} content in the silicate phases of the sintered product markedly increased but no Fe^{2+} or Fe^{3+} signal was found in the magnetite after heating at 700 °C. In addition, the ilmenite and the added np-Fe^0 might also provide sources for the increase in Fe^{2+} content in the silicate minerals. In general, the Fe^{2+}/Fe^{3+} ratio in sintered products of samples with np-Fe^0 was higher than that of samples without np-Fe^0 after heating at an equivalent temperature, suggesting that a reducing condition might be created by the addition of np-Fe^0, which is itself oxidized. Moreover, the abnormal ratio at 1000 °C might indicate that some silicates with low melting points melted, converting some Fe^{3+} into Fe^{2+} and transferring it to ilmenite or another silicate, thus increasing the ratio. However, this process already occurred in products of samples with np-Fe^0 at a lower temperature; thus, adding np-Fe^0 to the lunar soil simulant may also be responsible for the different Fe^{2+}/Fe^{3+} ratios in sintered products #1001 and #1002.

4.2. Implications for the microwave-sintering of lunar soil

In this study, the microstructure and composition of products were observed after the addition of np-Fe^0 to the lunar soil simulant CLRS-2, which coupled well with microwaves and converted microwave energy into thermal energy. Comparing the heated products showed that adding np-Fe^0 to the lunar soil simulant decreased the porosity and increased the density of sintered products at a given temperature. In addition, at lower temperatures, products of samples with np-Fe^0 presented similar properties to those of samples without np-Fe^0 at higher temperatures, suggesting that adding np-Fe^0 to the lunar soil simulant effectively improves the microwave-sintering rate. Because oxidation does not readily occur in the lunar environment, the microwave heating mechanism of np-Fe^0 in real lunar soil will be dominated by magnetic loss, thus the sintering efficiency will be better than that in the experiments. Studies of Apollo and CE-5 products indicate that np-Fe^0 is widely distributed in agglutinate glasses and the space weathering rims of lunar soil (Basu, 2005; Gu et al., 2022; Guo et al., 2022; Hapke, 2001; James et al., 2003; Pieters and Noble, 2016). The content of np-Fe^0 in lunar soil is generally 0.7–1.0 wt% and is higher in mature lunar mare soil. The space weathering rims, and agglutinate glass are transparent to microwaves, and have no specific melting point (Oghbaei and Mirzaee, 2010; Taylor and Meek, 2005); therefore, real lunar soil will melt and consolidate easily through transient liquid phases and the temperature increase caused by np-Fe^0 in the microwave-sintering process; this is illustrated in Fig. 8**.** It is foreseeable that np-Fe^0 will play an important role in the preparation of structural materials and hardening of the lunar surface for future lunar habitats through microwave-sintering technology. Because np-Fe^0 has a great absorbance capacity for microwaves, enabling volumetric heating at low temperature, and having energy-saving and time-saving characteristics, as well giving products with useful properties, microwaves could provide a promising technology to harden lunar soil for future infrastructure, including lunar research stations and roads, if a region with mature lunar soil is chosen.

5. Conclusions

In this paper, 1.0 wt% np-Fe^0 was added to the lunar soil simulant CLRS-2, and microwave-sintering experiments were conducted. The microstructure and composition of the heated products were subsequently analyzed. The results show that adding np-Fe^0 to the lunar soil simulant couples well with microwaves, causing a dense microstructure and evident changes in the composition of the products. From the similar characteristics of heated products at different temperatures, we suggest that the actual temperature in samples with np-Fe^0 might be increased, thus improving the microwave-sintering efficiency. At a temperature of 900 °C, product #0902 exhibited relatively hard properties. These parameters can guide the future preparation of structural materials and hardening of the lunar surface for creating a lunar habitat using microwave-sintering technology. Because adding np-Fe^0 to the lunar soil simulant demonstrates its favorable absorption properties in a microwave field, more attention should be paid to the microwave effects of np-Fe^0 in real lunar soil. In the future, the detailed mechanism of how adding np-Fe^0 to the lunar soil simulant promotes sintering in the microwave-sintering processes and the mechanical and thermal properties of sintered products should be further investigated.

Declaration of Competing Interest

The authors declare that they have no known competing financial interests or personal relationships that could have appeared to influence the work reported in this paper.

Acknowledgments

This work was funded by the Strategic Priority Research Program of Chinese Academy of Sciences [grant number XDB 41000000], National Natural Science Foundation of China [grant number 41931077], Youth Innovation Promotion Association CAS awards to Hong Tang [grant number 2018435], Technical Advanced Research Project of Civil Space [grant number D020201], Key Research Program of Frontier Sciences, CAS [QYZDY-SSW-DQC028]. The authors would like to thank Zongjun Yin, Suping Wu, Junhu Wang, Huiwen Zhou, Rier Ge, Xiandi Zeng, Jichao Fang, Yanhua Peng, and Chen Li for their technical support and experimental suggestions. We thank Martha Evonuk, PhD, and David Wacey, PhD, from Liwen Bianji (Edanz) (www.liwenbianji.cn/), for editing the English text of a draft of this manuscript.

Appendix A. Supplementary material

Supplementary data to this article can be found online at https://doi.org/10.1016/j.asr.2023.08.029.

References

Allan, S.M., Merritt, B.J., Griffin, B.F., Hintze, P.E., Shulman, H.S., 2013. High-temperature microwave dielectric properties and processing of JSC-1AC lunar simulant. J. Aerosp. Eng. 26, 874–881.

Anzulevich, A.P., Butko, L.N., Bychkov, I.V., et al., 2017. Dynamic magnetic losses in powders consisting of metallized dielectric particles at microwaves. J. Magn. Magn. Mater. 444, 307–312.

Basu, A., 2005. Nanophase Fe-0 in lunar soils. J. Earth Syst. Sci. 114, 375–380.

Cheng, J., Roy, R., Agrawal, D., 2002. Radically different effects on materials by separated microwave electric and magnetic fields. Mater. Res. Innov. 5, 170–177.

Duke, M.B., Blair, B.R., Diaz, J. Lunar resource utilization: Implications for commerce and exploration. In: Duke, M.B., (Ed.). Moon: Science, Exploration and Utilisation. 2413-9, 2003.

Dyar, M.D., Agresti, D.G., Schaefer, M.W., Grant, C.A., Sklute, E.C., 2006. Mössbauer spectroscopy of earth and planetary materials. Annu. Rev. Earth Planet. Sci. 34, 83–125.

El Khaled, D., Novas, N., Gazquez, J.A., Manzano-Agugliaro, F., 2018. Microwave dielectric heating: Applications on metals processing. Renew. Sustain. Energy Rev. 82, 2880–2892.

Farries, K.W., Visintin, P., Smith, S.T., Eyk, P.v., 2021. Sintered or melted regolith for lunar construction: state-of-the-art review and future research directions. Constr. Build. Mater. 296.

Fateri, M., Gebhardt, A., 2015. Process parameters development of selective laser melting of lunar regolith for on-site manufacturing applications. Int. J. Appl. Ceram. Technol. 12, 46–52.

Gu, L., Chen, Y., Xu, Y., et al., 2022. Space weathering of the Chang'e-5 lunar sample from a mid-high latitude region on the moon. Geophys. Res. Lett. 49.

Guo, Z., Li, C., Li, Y., et al., 2022. Nanophase iron particles derived from fayalitic olivine decomposition in Chang'E-5 lunar soil: Implications for thermal effects during impacts. Geophys. Res. Lett. 49.

Gupta, M., Wong, W.L.E. Microwaves and Metals (Gupta/Microwaves and Metals) || Index. 2007.

Hapke, B., 2001. Space weathering from Mercury to the asteroid belt. J. Geophys. Res. Planets 106, 10039–10073.

Hapke, B., Cassidy, W., Wells, E., 1975. Effects of vapor-phase deposition processes on the optical, chemical, and magnetic properties OE the lunar regolith. The Moon 13, 339–353.

Herzenberg, C.L., 1970. Mössbauer spectrometry as an instrumental technique for determinative mineralogy. Mössbauer effect methodology. Springer, pp. 209–230.

Herzenberg, C.L., Riley, D.L., 1970. Mössbauer spectrometry of lunar samples. Science 167, 683–1000.

Herzenberg, C.L., Riley, D.L., 1971. Analysis of returned lunar samples by techniques based on Mössbauer spectrometry. Phys. Earth Planet. In. 4, 204–214.

Hill, E., Taylor, L.A., Liu, Y., Day, J.M.D., 2005. Microwave processing of lunar soil simulants JSC-1 and MLS-1. Meteorit. Planet. Sci. 5197.

James, C., Letsinger, S., Basu, A., Wentworth, S., McKay, D. Nanophase Iron Globules in Lunar Soil. Lunar and Planetary Science Conference. pp. 1992, 2003.

Kim, Y.-J., Ryu, B.H., Jin, H., Lee, J., Shin, H.-S., 2021. Microstructural, mechanical, and thermal properties of microwave-sintered KLS-1 lunar regolith simulant. Ceram. Int. 47, 26891–26897.

Lei, S., Jiao, X., Hong, T., et al., 2020. Vacuum sintering behavior and magnetic transformation for high-Ti type basalt simulated lunar regolith. Icarus.

Lim, S., Anand, M., 2019. Numerical modelling of the microwave heating behaviour of lunar regolith. Planet. Space Sci. 179 104723.

Lim, S., Bowen, J., Degli-Alessandrini, G., Anand, M., Cowley, A., Levin Prabhu, V., 2021. Investigating the microwave heating behaviour of lunar soil simulant JSC-1A at different input powers. Sci. Rep. 11.

Loeffler, M., Dukes, C., Baragiola, R., 2009. Irradiation of olivine by 4 keV He+: Simulation of space weathering by the solar wind. J. Geophys. Res. Planets 114.

Luo, J., Hunyar, C., Feher, L., Link, G., Thumm, M., Pozzo, P., 2004. Theory and experiments of electromagnetic loss mechanism for microwave heating of powdered metals. Appl. Phys. Lett. 84, 5076–5078.

Mo, B., Guo, Z., Li, Y., et al., 2022. In situ investigation of the valence states of iron-bearing phases in Chang'E-5 lunar soil using FIB, AES, and TEM-EELS techniques. At. Spectrosc. 43, 53–59.

Mondal, A., Agrawal, D., Upadhyaya, A., 2008. Microwave heating of pure copper powder with varying particle size and porosity. J. Microw. Power Electromagn. Energy : Publication Int. Microw. Power Inst. 43, 5–10.

Mondal, A., Shukla, A., Upadhyaya, A., Agrawal, D., 2010. Effect of porosity and particle size on microwave heating of copper. Sci. Sinter. 42, 169–182.

Morris, R., 1980. Origins and size distribution of metallic iron particles in the lunar regolith. Lunar Planet. Sci. Conf. Proc., 1697–1712

Nakamura, T., Senior, C.L. Solar thermal power system for lunar ISRU processes. Space Technology and Applications International Forum. Albuquerque, NM, pp. 1206-15, 2005.

Nakamura, T., Senior, C.L., 2008. Solar thermal power for lunar materials processing. J. Aerosp. Eng. 21, 91–101.

Oghbaei, M., Mirzaee, O., 2010. Microwave versus conventional sintering: A review of fundamentals, advantages and applications. J. Alloy. Compd. 494, 175–189.

Pieters, C.M., Noble, S.K., 2016. Space weathering on airless bodies. J. Geophys. Res. Planets 121, 1865–1884.

Rancourt, D., Ping, J., Berman, R., 1994. Mössbauer spectroscopy of minerals. Phys. Chem. Miner. 21, 258–267.

Rybakov, K.I., Semenov, V.E., Egorov, S.V., Eremeev, A.G., Plotnikov, I.V., Bykov, Y.V., 2006. Microwave heating of conductive powder materials. J. Appl. Phys. 99.

Rybakov, K.I., Volkovskaya, I.I., 2019. Electromagnetic field effects in the microwave sintering of electrically conductive powders. Ceram. Int. 45, 9567–9572.

Sasaki, S., Nakamura, K., Hamabe, Y., Kurahashi, E., Hiroi, T., 2001. Production of iron nanoparticles by laser irradiation in a simulation of lunar-like space weathering. Nature 410, 555–557.

Srivastava, V., Lim, S., Anand, M., 2016. Microwave processing of lunar soil for supporting longer-term surface exploration on the Moon. Space Policy 37, 92–96.

Stevens, J.G., Khasanov, A.M., Pollak, H., Zhe, L. Mössbauer mineral handbook. Mössbauer Effect Data Center Asheville, 1998.

Sun, J., Wang, W., Yue, Q. Review on Microwave-Matter Interaction Fundamentals and Efficient Microwave-Associated Heating Strategies. Materials 9, 2016.

Tang, H., Li, X., Wang, S., Li, Y., 2011. The origin and simulation of nanophase iron in lunar soil. Adv. Earth Sci. 26, 507–515.

Taylor, L.A., Meek, T.T., American astronautical, s. Microwave processing of lunar soil. International Lunar Conference 2003/International Lunar Exploration Working Group 5 Conference. Waikoloa, HI, pp. 109-23, 2003.

Taylor, L., Hill, E., Liu, Y., Park, J., Bruce, R. Microwave processing Apollo soil: products for a lunar base. Earth & Space 2006: Engineering, Construction, and Operations in Challenging Environment. 1-8, 2006.

Taylor, L.A., Liu, Y. Important considerations for lunar soil simulants. Earth and Space 2010: Engineering, Science, Construction, and Operations in Challenging Environments. 106-18, 2010.

Taylor, L.A., Meek, T.T., 2005. Microwave sintering of lunar soil: Properties, theory, and practice. J. Aerosp. Eng. 18, 188–196.

Vinothini, V., Vaidhyanathan, B., Binner, J., 2010. Microwave assisted synthesis of barium zirconium titanate nanopowders. J. Mater. Sci.

Weber, I., Stojic, A.N., Morlok, A., et al., 2020. Space weathering by simulated micrometeorite bombardment on natural olivine and pyroxene: A coordinated IR and TEM study. Earth Planet. Sci. Lett. 530 115884.

Whittaker, A.G., Mingos, D.M.P. Microwave-assisted solid-state reactions involving metal powders. Journal of the Chemical Society-Dalton Transactions, 2073-9, 1995.

Whittaker, A.G., Mingos, D.M.P., 1993. Microwave-assisted solid-state reactions involving metal powders and gases. J. Chem. Soc. Dalton Trans.

Yamada, M., Sasaki, S., Nagahara, H., et al., 1999. Simulation of space weathering of planet-forming materials: Nanosecond pulse laser irradiation and proton implantation on olivine and pyroxene samples. Earth Planets Space 51, 1255–1265.

Yun, H.-S., Yun, B.-G., Lee, H.-M., Jeong, D.-Y., Lee, W.-I., Cho, N.-H., 2019. Low-temperature synthesis of nanoscale BaTiO3 powders via microwave-assisted solid-state reaction. SN Appl. Sci. 1, 1–9.

Zhang, Y., Agrawal, D.K., Cheng, J., Slawecki, T., 2018. Microwave power absorption mechanism of metallic powders. IEEE Trans. Microw. Theory Tech. 66, 2107–2115.

Zhang, X., Khedmati, M., Kim, Y.-R., et al., 2020. Microstructure evolution during spark plasma sintering of FJS-1 lunar soil simulant. J. Am. Ceram. Soc. 103, 899–911.

Zhang, X., Gholami, S., Khedmati, M., et al., 2021. Spark plasma sintering of a lunar regolith simulant: effects of parameters on microstructure evolution, phase transformation, and mechanical properties. Ceram. Int. 47, 5209–5220.

Zhou, C., Tang, H., Li, X., et al., 2021. Effects of ilmenite on the properties of microwave-sintered lunar regolith simulant. J. Aerosp. Eng. 34.

Zhou, Y., Wang, W., Sun, J., et al., 2017. Direct calorimetry study of metal discharge heating effects induced by microwave irradiation. Appl. Therm. Eng. 125, 386–393.